RESEARCH ARTICLE | MAY 19 2014

Electrode of ionic polymer-metal composite sensors: Modeling and experimental investigation

Qi Shen; Kwang J. Kim; Tianmiao Wang

J. Appl. Phys. 115, 194902 (2014)
https://doi.org/10.1063/1.4876255

JOURNAL OF APPLIED PHYSICS 115, 194902 (2014)

Electrode of ionic polymer-metal composite sensors: Modeling and experimental investigation

Qi Shen,[1,2] Kwang J. Kim,[2] and Tianmiao Wang[1]

[1]*Robotic Institute, School of Mechanical Engineering and Automation, Beihang University, Beijing 100191, China*

[2]*Active Materials and Smart Living (AMSL) Laboratory, Mechanical Engineering Department, University of Nevada-Las Vegas, Las Vegas, Nevada 89154-4027, USA*

(Received 25 February 2014; accepted 25 April 2014; published online 19 May 2014)

In this study, we theoretically model and experimentally investigate the electrode electrical properties and the mechano-electrical properties of the ionic polymer-metal composite (IPMC) sensor. A physics-based model of the electrode was developed. In addition, based on the Poisson-Nernst-Planck system of equations, the current in the polymer membrane was modeled. By combining the physics of the polymer membrane and the electrode, the model of the surface electrical potential of the IPMC sensor was proposed. Experiments were conducted to test the electrical characteristics of the electrode and validate the model. The results demonstrate that the model can well describe the resistance, capacitance, and surface electrical potential of the IPMC electrode under external oscillation. Based on the model, a parametric study was done to investigate the impact of the parameters on the IPMC electrode properties. The results show that by changing the parameters of the electrode, such as the particle diameter, the electrode thickness, and microstructure, the electrical properties of the electrode can be changed accordingly. The current method of examining the electrode properties may also be applied to the study of electrodes for other smart materials. [http://dx.doi.org/10.1063/1.4876255]

I. INTRODUCTION

The study of smart materials has significantly attributed to the development of underwater sensors and actuators.[1–12] The ionic polymer-metal composite (IPMC) is one of the promising smart materials used for soft underwater sensing.[13–19] It is made of an ionic polymer membrane with chemically plated gold or platinum acting as electrodes on both sides.[20,21] The most interesting characteristics of IPMC are its softness, lightness, and unique ability to deform under the presence of an applied electric field, due to ion redistribution in the polymer membrane. As a result, actuated biomimetic underwater robots have been widely studied. Furthermore, the IPMC is capable of generating a detectable voltage if subjected to a mechanical deformation as a result of ion distribution in the polymer membrane. This characteristic allows the application of IPMC as soft sensors in force, pressure, and displacement measurements.

Many works concerning the actuating performance of IPMC have been reported. De Gennes *et al*. presented a model that describes the effect of an applied electric field on the spontaneous curvature and an imposed curvature on the electric field.[22] Shahinpoor and Kim found that electrode conductivity has an influence on the transduction behavior of IPMC.[23] Nemat-Nasser and Li first proposed a model that describes mechanoelectrical transduction in relation to the electrostatic interaction within the polymer.[24] The underlying cause of the actuation is explained by the internal stress induced by the interaction between the ion pairs inside a cluster. Chen and Tan investigated the electrical dynamics of the IPMC based on Nemat-Nasser's work.[25] They expanded the model and added the effect of surface resistance. Recently, Porfiri showed that the electrodes do significantly affect the charge dynamics and hence the actuation performance of IPMC.[26] Pugal *et al*. developed a physics based model that couples the currents in the polymer to the electric current in the continuous electrodes of IPMC.[27]

In comparison to the extensive work on the actuating performance, studies on the IPMC sensing performance have been limited. As early as 1996, Shahinpoor first discovered the sensing capabilities of IPMCs.[28] The phenomenon of flexogelectric effect in connection with dynamic sensing of ionic polymeric gels was discussed. Shahinpoor *et al*. also discussed the potential applications of IPMCs as biomimetic sensors.[29–31] The sensing capabilities of IPMC were investigated, and it was found that IPMCs are highly capacitive at low frequencies, while they are highly resistive under high frequency excitations.[32] IPMC sensors were also designed to measure the blood pressure, pulse rate, and rhythm.[33] Chemical processes of fabricating IPMCs and IPMC variations suitable for applications of fuel cells, electrolysis, and hydrogen sensors were also discussed.[34] Farinholt and Leo developed a charge sensing model of IPMC sensors based on Nemat-Nasser's model which indicates that induced stress will produce a capacitive discharge in the polymer.[35] Bonomo *et al*. conducted a systematic study on the IPMC as a motion sensor.[36] Chen *et al*. presented a dynamic model for IPMC sensors which relates a short-circuit sensing current to an applied deformation.[37] Aureli and Porfiri developed a chemo-electromechanical model for the IPMC in response to the mechanical deformations. The model is derived from the Poisson-Nernst-Planck equations and describes the impact of the voltage field and the counterion concentration on the IPMC.[38] The energy harvester capabilities of the IPMC were also investigated.[39] Kim *et al.* geometrically modeled the electrode of the IPMC and estimated the impedance properties of the electrode based on the previously noted parametric studies.[40] However, the current model cannot describe the impedance of the electrode well due to the limitation of the estimations of the curved electrode's properties. To date, few studies have been done on the electrical characteristics of the IPMC electrodes.

The goal of this paper is to study the electrical properties of the IPMC electrode. First, a microstructure model of the electrode was developed. The model describes the metal particle arrangement-microstructure in the electrode. The arrangement of particles used in this model was inspired by the primary metallic crystal structures (i.e., the face-centered cubic (FCC), body-centered cubic (BCC), and hexagonal close packed (HCP) structure).[41–44] The model started from a basic cubic and was expanded to include vacancy defects. Based on the volume change of the electrode caused by the IPMC beam bending, the variation of the resistance and capacitance of the IPMC was obtained. Second, a physical model of the membrane was proposed based on the Ramo-Shockley theorem[45,46] and was used to calculate the current in the continuous electrodes of the IPMC. Finally, the electric potential of the electrodes was obtained by combing the model of the surface electrode and the polymer membrane.

In addition, experiments were conducted to identify the model parameters and validate the theoretical model. A scanning electron microscope (SEM) was used to study the microstructure of the IPMC. An experimental apparatus was implemented. The resistance, capacitance, and surface potential of the electrode were measured. Based on the results, the parameters in the proposed model were identified. The theoretical results were compared with the experimental results to verify the model.

The parametric studies were performed for a comprehensive understanding of the electric properties of the IPMC electrode, and the impact of the parameters on the IPMC electrode properties was obtained. Different microstructures of the electrode were also modeled, and the simulation results were presented. Current model can be extended to the model to explaining the mechanoelectrical phenomenon of IPMC. The surface voltage of the IPMC can be used to sense the deformation. The current study is also beneficial for the sensing performance of the IPMC by varying the electrical characteristics of the electrode.

The rest of this paper is organized as follows: a physical-based model of the IPMC sensor electrode is developed in Sec. II; experimental results and comparisons with the model prediction are presented in Sec. III; discussion on the electric properties of the IPMC electrode is presented in Sec. IV; and Sec. V is the conclusion.

II. MODELING OF IPMC SENSOR ELECTRODE

A. Microstructure model of the electrodes

In this section, we focus on the electrical properties of the IPMC electrode. The model of the resistance and capacitance was developed. Previous work reported that the coagulation of the platinum atoms is generated through the electroless plating process.[20,21] The incipient particles, with diameters less than 10 nm, coagulate during the reduction process and eventually grow to 50–100 nm. It is assumed that the electrode satisfies the following restrictions: (1) The coagulated platinum particles are spherical and conserve the electrical properties of platinum; (2) during the deformation of the electrode, the distance between the metal particles and the size of the cube changes accordingly; (3) the electrode of the IPMC consists of two parts: the metal particles and the voids between the particles; (4) the upper part of the electrode, which mainly results in the resistance, and the inner electrode, which results in the capacitance, form the layer of the electrode.[47] The arrangement of particles in the electrodes was assumed to have three kinds of structure: the FCC, the BCC, and the HCP structure. The reason of using unit cell for defining the particle arrangement is that the impedance of the electrode can be calculated conveniently by integrating the unit cell in the three dimensions along with the defective cell. In addition, the influence of the deformation can result in the changing of the cell size. The model of the electrode, which describes the metal particle arrangement-microstructure, is developed based on these three structure forms separately. The vacancy defect was also included in the model. Figure 1 shows the schematic drawing of the three forms.

1. Resistance

We assume the tip displacement of the IPMC is much smaller than its length, and the IPMC is assumed to bend vertically at the tip denoted by $\nu(t)$. The length and width

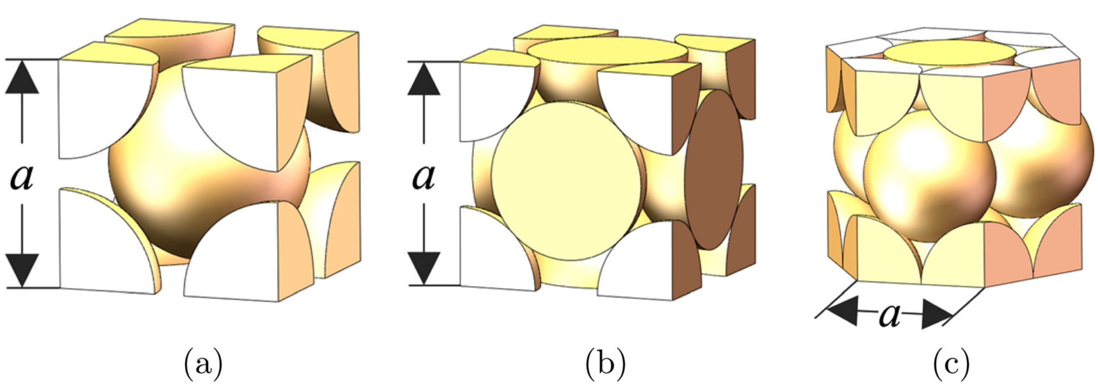

FIG. 1. Three common microstructures of metal: (a) The body-centered cubic; (b) the face-centered cubic; (c) the hexagonal closed packed structure.

thickness of the IPMC beam is L and W. The thickness of the membrane and electrode is $2h$ and h_e. See Fig. (2). The radius of the curved IPMC midline can be expressed as

$$r(t) = \frac{L}{\gamma(t)}, \tag{1}$$

where γ is the angle of the curved IPMC and is donated as

$$\tan\gamma(t) = \frac{\nu(t)}{L}. \tag{2}$$

Take unit cell of the electrode as an example. The length of the midline in relative with the cube is assumed as dz. The angle of the cube is written as

$$d\gamma(t) = \frac{dz}{r(t)}. \tag{3}$$

The length of the stretched electrode can be expressed as

$$dL(t) = d\gamma(t)(r(t) + h + \hat{h}), \tag{4}$$

where $\hat{h}$ is the position of the cube along the thickness direction of the electrode. We study the FCC first. Two kinds of cubes are considered: the normal cube and the cube with a vacancy defect. The side length of cube, a, and the distance between the layers, h_0, can be denoted as[40]

$$a = \sqrt{2}D, \quad h_0 = \frac{\sqrt{6}}{3}D, \tag{5}$$

where D is the diameter of the particle. Next, we consider the contact area between the particles. The number of particles in the electrode can be determined by $n = N_t \cdot N_w \cdot N_l$. N_t, N_w, N_l are the number of layers in the x, y, z direction and can be expressed as[40]

$$\begin{aligned} N_t &= \frac{\sqrt{6}}{2}\frac{h_e - D}{\acute{D}} + 1, \quad N_w = \frac{2\sqrt{3}}{3}\frac{W-D}{\acute{D}} + 1, \\ N_l &= \frac{L-D}{\acute{D}} + 1, \end{aligned} \tag{6}$$

with

$$\acute{D} = D\sqrt{1 - f^2},$$

where f is the contact area ratio.[40] The number of the voids and the size of the void cube in the electrode is

$$n_v = \frac{Lh_eW}{g_v^3}, \quad s_v = \hat{s}_v \cdot \frac{dL(t)}{dz} = \hat{s}_v \frac{r(t) + h + \hat{h}}{r(t)}, \tag{7}$$

with

$$\hat{s}_v = \sqrt[3]{\frac{V_v}{n_v}},$$

where V_v and g_v are the volume of the void and the gaps between the centers of the voids.[40] The resistance of the normal cube can be expressed as

$$\begin{aligned} \Delta R_n(t) &= \frac{\rho_p(a - 2s_v)}{a^2}\frac{r(t) + h + \hat{h}}{r(t)} \\ &\quad + \frac{2\rho_p\rho_v s_v}{2\rho_p s_v^2 + \rho_v(a^2 - 2s_v^2)}\frac{r(t) + h + \hat{h}}{r(t)}, \end{aligned} \tag{8}$$

where ρ_p and ρ_v are the resistivity of the particle and void. In the current study, the IPMC is hydrated and the void is water. We assume the particle in the center of the defective cube is missing, as shown in Fig. 3(a). The resistance of the defective cube can be expressed as

$$\begin{aligned} \Delta R_d(t) &= \frac{\rho_p(a - s_v)}{a^2}\frac{r(t) + h + \hat{h}}{r(t)} \\ &\quad + \frac{\rho_p\rho_v s_v}{2\rho_p s_v^2 + \rho_v(a^2 - 2s_v^2)}\frac{r(t) + h + \hat{h}}{r(t)}. \end{aligned} \tag{9}$$

Then we integrate the resistance of the cube (see Eqs. (8) and (9)) in the z, y, x direction separately. The reciprocal of the electrode resistance $R_e(t)$ can be obtained as follows:

$$\begin{aligned} \Delta R_z(t) &= \int_0^L (1 - P_z)\Delta R_n(t)\frac{dL}{a} + \int_0^L P_z \Delta R_d(t)\frac{dL}{a} \\ &= \frac{EL}{a}(r(t) + h + \hat{h}), \end{aligned} \tag{10}$$

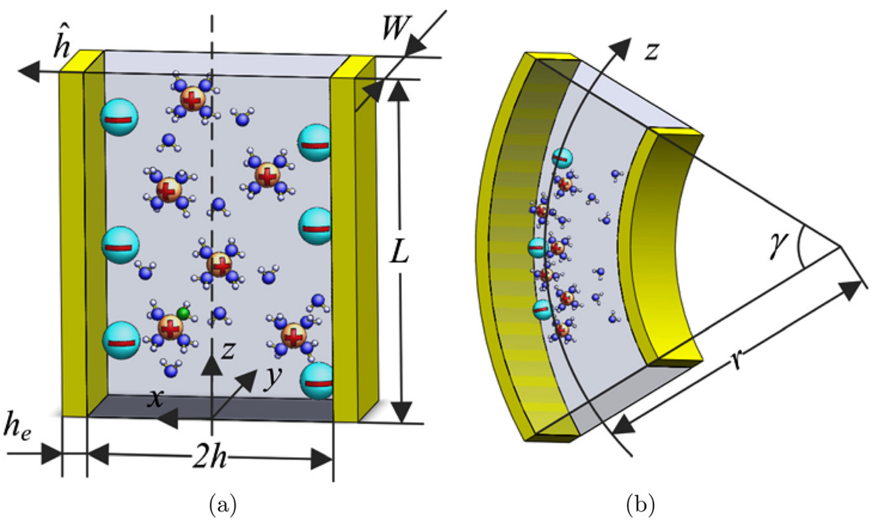

FIG. 2. Schematic illustration of IPMC beam: (a) Dimensions of the IPMC; (b) IPMC with the bending radius.

$$\frac{1}{\Delta R_y(t)} = \int_0^W \frac{1-P_y}{E(r(t)+h+\hat{h})L/a}\frac{dW}{a} + \int_0^W \frac{P_y}{\frac{G}{r(t)}(r(t)+h+\hat{h})L/a}\frac{dW}{a}, = \frac{J}{r(t)+h+\hat{h}}, \tag{11}$$

$$\frac{1}{R_e(t)} = \int_0^{h_e} J\frac{1-P_x}{r(t)+h+\hat{h}}\frac{d\hat{h}}{a} + \int_0^{h_e}\frac{P_x r(t)}{G(r(t)+h+\hat{h})L/W}\frac{d\hat{h}}{a}, = \left(J\frac{1-P_x}{a}+\frac{P_xWr(t)}{GaL}\right)\ln\frac{r(t)+h+\hat{h}}{r(t)+h}, \tag{12}$$

where

$$E = \frac{F(1-P_z)}{r(t)} + \frac{GP_z}{r(t)},$$
$$F = \frac{\rho_p(a-2s_v)}{a^2} + \frac{2\rho_p\rho_v s_v}{2\rho_p s_v^2+\rho_v(a^2-2s_v^2)},$$
$$G = \frac{\rho_p(a-s_v)}{a^2} + \frac{\rho_p\rho_v s_v}{2\rho_p s_v^2+\rho_v(a^2-2s_v^2)},$$
$$J = \frac{(1-P_y)W}{EL} + \frac{P_yWr(t)}{GL},$$

where h_e is the thickness of the electrode, and P_x, P_y, P_z are the percentages of the defective cube in the x, y, z direction. By inverting Eq. (12), the resistance of the electrode is obtained. The percentage of the vacancy can be expressed as

$$P_v = \frac{1}{2}(1-(1-P_x)(1-P_y)(1-P_z)). \tag{13}$$

The resistance of the BCC and HCP structure can be calculated by using a similar method. The side length of cube, a, and the distance between the layers, h_0, of the BCC can be denoted as

$$a = \frac{2\sqrt{3}}{3}D, \quad h_0 = \frac{\sqrt{3}}{3}D. \tag{14}$$

The number of layers of the BCC in the x, y, z direction can be expressed as

$$N_t = \frac{\sqrt{3}}{3}\frac{h_e-D}{\acute{D}}+1, \quad N_w = \frac{\sqrt{3}}{2}\frac{W-D}{\acute{D}}+1, \quad N_l = \frac{\sqrt{3}}{2}\frac{L-D}{\acute{D}}+1. \tag{15}$$

We assume the particle in each side of the defective cube is missing. See Fig. 3(b). The resistance of the normal and defective BCC can be expressed as

$$\Delta R_n(t) = \frac{\rho_p(a-2s_v)}{a^2}\frac{r(t)+h+\hat{h}}{r(t)} + \frac{\rho_p\rho_v s_v}{\rho_p s_v^2+\rho_v(a^2-s_v^2)}\frac{r(t)+h+\hat{h}}{r(t)} + \frac{\rho_p\rho_v s_v}{2\rho_p s_v^2+\rho_v(a^2-2s_v^2)}\frac{r(t)+h+\hat{h}}{r(t)} \tag{16}$$

and

$$\Delta R_d(t) = \frac{\rho_p(a-s_v)}{a^2}\frac{r(t)+h+\hat{h}}{r(t)} + \frac{\rho_p\rho_v s_v}{\rho_p s_v^2+\rho_v(a^2-s_v^2)}\frac{r(t)+h+\hat{h}}{r(t)}. \tag{17}$$

Then by integrating the resistance of the cube (see Eqs. (16) and (17)) in the z, y, x direction, the resistance of the electrode can be obtained. The side length of the hexagon, a, and the distance between the layers, h_0, of the HCP structure can be denoted as

$$a = D, \quad h_0 = 0.82D. \tag{18}$$

The unit cell of the HCP structure can be converted to a rectangle to simplify. The number of layers of the HCP structure in the x, y, z direction can be expressed as

$$N_t = 1.23\frac{h_e-D}{\acute{D}}+1, \quad N_w = \frac{2}{3}\frac{W-D}{\acute{D}}+1, \quad N_l = \frac{L-D}{\acute{D}}+1. \tag{19}$$

We assume the particles in the center and in the top and bottom side of the defective cube is missing. See Fig. (3). The resistance of the normal cube and the defective cube of the HCP structure can be expressed as

$$\Delta R_n(t) = \frac{2\rho_p(\sqrt{3}a-2s_v)}{3as_v}\frac{r(t)+h+\hat{h}}{r(t)} + \frac{3\rho_p\rho_v s_v}{2\rho_p s_v^2+\rho_v(3as_v-2s_v^2)}\frac{r(t)+h+\hat{h}}{r(t)} \tag{20}$$

and

$$\Delta R_d(t) = \frac{\sqrt{3}\rho_p}{3h_0}\frac{r(t)+h+\hat{h}}{r(t)} + \frac{\sqrt{3}\rho_p\rho_v a}{3\rho_p as_v+3\rho_v(h_0-s_v)}\frac{r(t)+h+\hat{h}}{r(t)}. \tag{21}$$

Through integrating the resistance of the unit cell (see Eqs. (20) and (21)) in the z, y, x direction, the resistance of the electrode can be obtained.

2. Capacitance

The capacitor was formed in the inner electrode layer of the IPMC, which was between the electrode layer and the polymer membrane. Since the particles of the upper electrode layer were connected, the upper layer cannot form a capacitor.[40] The method to calculate the capacitance of the electrode is the same as that of the resistance. The capacitance of the normal cube of the FCC can be expressed as

$$\Delta C_n(t) = \frac{3\varepsilon\hat{s}_v^2}{\tilde{s}_v}\frac{r(t)+h+\hat{h}}{r(t)}, \tag{22}$$

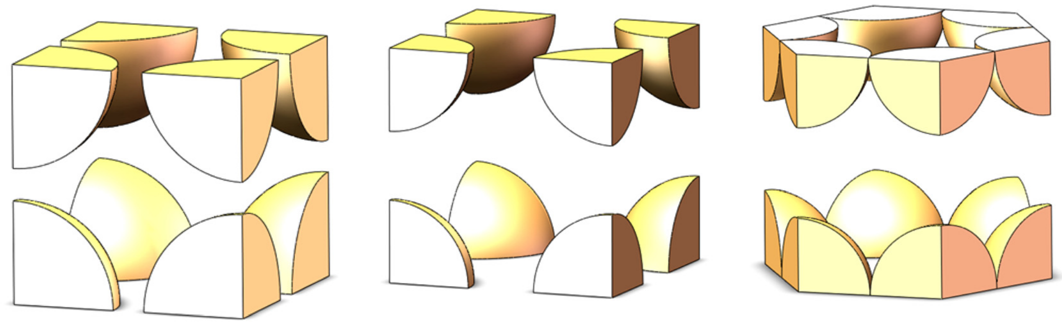

(a) (b) (c)

FIG. 3. Vacancy defects in primary metallic microstructures: (a) The body-centered cubic; (b) the face-centered cubic; (c) the hexagonal closed packed structure.

with

$$\tilde{s}_v = \frac{\sqrt{2}\hat{a}\hat{s}_v}{2D}, \quad \hat{a} = \sqrt{2}(g_p + D),$$

where ε is the dielectric constant and g_p is the distance between the surface of particles. The capacitance of the defective cube (see Fig. 3(a)) can be expressed as

$$\Delta C_d(t) = \frac{\varepsilon\hat{s}_v^2}{\tilde{s}_v}\frac{r(t)+h+\hat{h}}{r(t)}. \tag{23}$$

By integrating the capacitance of the electrode cube in the z, y, x direction, one can obtain the reciprocal of the electrode capacitance $C_e(t)$ as follows:

$$\begin{aligned}\Delta C_z(t) &= \int_0^L (1-\hat{P}_z)\Delta C_n(t)\frac{dL}{\hat{a}} + \int_0^L \hat{P}_z\Delta C_d(t)\frac{dL}{\hat{a}}\\ &= \hat{E}\frac{L}{\hat{a}}(r(t)+h+\hat{h}),\end{aligned} \tag{24}$$

$$\begin{aligned}\Delta C_y(t) &= \int_0^W \hat{E}(1-\hat{P}_y)(r(t)+h+\hat{h})\frac{L}{\hat{a}}\frac{dW}{\hat{a}}\\ &\quad+\int_0^W \hat{P}_y\frac{\hat{G}}{r(t)}(r(t)+h+\hat{h})\frac{L}{\hat{a}}\frac{dW}{\hat{a}}\\ &= \hat{J}(r(t)+h+\hat{h}),\end{aligned} \tag{25}$$

$$\begin{aligned}\frac{1}{C_e(t)} &= \int_0^{\hat{h}_e}\frac{1-\hat{P}_x}{J(r(t)+h+\hat{h})}\frac{d\hat{h}}{a} + \int_0^{\hat{h}_e}\frac{\hat{P}_x r(t)}{\hat{G}LW/\hat{a}^2}\frac{d\hat{h}}{\hat{a}},\\ &= \left(\frac{1-\hat{P}_x}{\hat{J}\hat{a}} + \frac{\hat{P}_x\hat{a}r(t)}{\hat{G}LW}\right)\ln\frac{r(t)+h+\hat{h}_e}{r(t)+h},\end{aligned} \tag{26}$$

with

$$\hat{E} = \frac{\hat{F}(1-\hat{P}_z)}{r(t)} + \frac{\hat{G}\hat{P}_z}{r(t)}, \quad \hat{F} = \frac{3\varepsilon\hat{s}_v^2}{\tilde{s}_v},$$

$$\hat{G} = \frac{\varepsilon\hat{s}_v^2}{\tilde{s}_v}, \quad \hat{J} = \frac{(1-\hat{P}_y)\hat{E}LW}{\hat{a}^2} + \frac{\hat{P}_y\hat{G}LW}{\hat{a}^2 r(t)},$$

where $\hat{h}_e$ is the thickness of the inner electrode, and $\hat{P}_x$, $\hat{P}_y$, $\hat{P}_z$ are the percentages of defective cubes in the x, y, z direction. By inversing Eq. (26), the expression of the capacitance of the electrode can be obtained. The percentage of the vacancy can be expressed as

$$\hat{P}_v = \frac{1}{2}(1-(1-\hat{P}_x)(1-\hat{P}_y)(1-\hat{P}_z)). \tag{27}$$

The capacitance of the BCC and HCP structure can be calculated in a similar method. The capacitance of the normal cube and the defective cube of the BCC can be expressed as

$$\Delta C_n(t) = \frac{5\varepsilon\hat{s}_v^2}{2\tilde{s}_v}\frac{r(t)+h+\hat{h}}{r(t)}, \tag{28}$$

$$\Delta C_d(t) = \frac{2\varepsilon\hat{s}_v^2}{\tilde{s}_v}\frac{r(t)+h+\hat{h}}{r(t)}, \tag{29}$$

with

$$\tilde{s}_v = \frac{\sqrt{3}\hat{a}\hat{s}_v}{2D}, \quad \hat{a} = \frac{\sqrt{3}}{3}(g_p + D).$$

Then by integrating the capacitance of the cube (see Eqs. (28) and (29)) in the z, y, x direction, the capacitance of the electrode can be obtained. The capacitance of the normal cube and the defective cube of the HCP structure can be expressed as

$$\Delta C_n(t) = \frac{3\varepsilon\hat{s}_v^2}{h_0}\frac{r(t)+h+\hat{h}}{r(t)}, \tag{30}$$

$$\Delta C_d(t) = \frac{\varepsilon\hat{a}^2}{h_0}\frac{r(t)+h+\hat{h}}{r(t)}, \tag{31}$$

with

$$\hat{a} = \frac{2\sqrt{3}}{3}(g_p + D).$$

Through integrating the capacitance of the unit cell (see Eqs. (30) and (31)) in the z, y, x direction, the capacitance of the electrode can be obtained.

B. Model of the polymer membrane

The cation migration and diffusion in the polymer backbone are calculated using the Nernst-Planck equation[24]

$$\frac{\partial C}{\partial t} + \nabla \cdot (-D\nabla C - \hat{z}\mu F C \nabla \phi) = 0, \quad (32)$$

where C is the cation concentration, μ is the mobility of cations, D is the diffusion constant, F is the Faraday constant, $\hat{z}$ is the charge number, and ϕ is the electric potential in the polymer. As ions cannot move beyond the boundary of the polymer, a local non-zero charge concentration starts to form near the surface of the platinum electrodes, which in turn results in an increase of an electric field in the opposite direction. This is described with Poisson's equation

$$\nabla \cdot \vec{E} = -\nabla^2 \phi = \frac{\rho}{\hat{\varepsilon}}, \quad (33)$$

where $\hat{\varepsilon}$ is the absolute dielectric constant $\hat{\varepsilon} = 0.2 \times 10^{-3}\mathrm{F/m}$, $\vec{E}$ is the strength of the electric field, and ρ is the charge density defined as

$$\rho = F(C - C_0), \quad (34)$$

where C_0 is the constant anion concentration $C_0 = 1200\,\mathrm{mol/m^3}$. By substituting Eqs. (33) and (34) into (32), Eq. (32) can be rewritten as

$$\frac{\partial C}{\partial t} + \nabla \cdot (-D\nabla C - \hat{z}\mu(\hat{\varepsilon}\nabla E + FC_0)\nabla \phi) = 0. \quad (35)$$

Since $\hat{\varepsilon}\nabla E \ll FC_0$,[37] Eq. (35) is expressed as

$$\frac{\partial C}{\partial t} + \nabla \cdot (-D\nabla C - \hat{z}\mu F C_0 \nabla \phi) = 0. \quad (36)$$

By combing Eqs. (33), (34), and (36), one can obtain

$$\frac{\partial \rho}{\partial t} - D\frac{\partial^2 \rho}{\partial x^2} + \frac{\hat{z}\mu F^2 C_0}{\hat{\varepsilon}}\rho = 0. \quad (37)$$

Performing a Laplace transform for the time variable of $\rho(x, z, t)$, one converts Eq. (37) into the Laplace domain

$$\rho(x,z,t)s - D\frac{\partial^2 \rho(x,z,t)}{\partial x^2} + \frac{\hat{z}\mu F^2 C_0}{\hat{\varepsilon}}\rho(x,z,t) = 0. \quad (38)$$

In particular, it is assumed that the charge density, $\rho(\pm h, z, s)$, at the boundary of $x = \pm h$ is proportional to the induced stress $\sigma(\pm h, z, s)$.[24] Therefore

$$\sigma(\pm h, z, s) = \alpha\rho(\pm h, z, s). \quad (39)$$

Considering the boundary condition $\rho(h, z, s) + \rho(-h, z, s) = 0$, $\rho(x, L, s) = 0$ and by solving Eq. (38), one can obtain

$$\rho(x,z,s) = 2\hat{C}(s)(L-z)\sinh(A(s)x), \quad (40)$$

where

$$A(s) = \sqrt{\frac{B+s}{D}},$$
$$B(s) = \frac{\hat{z}\mu F^2 C_0}{\hat{\varepsilon}}.$$

By relating $\sigma(\pm h, z, s)$ to external stimuli, one can obtain[37]

$$\hat{C}(s) = \frac{3Yh}{2\alpha L^3 W \sinh(A(s)h)}\nu(s), \quad (41)$$

where Y is the Young's modulus of the IPMC beam. Using Eqs. (33), (40), and (41), the expression for the electric field is

$$E(x,z,s) = 2\hat{C}(s)\frac{(L-z)\cosh(A(s)x)}{\hat{\varepsilon}A(s)} + a(z,s), \quad (42)$$

where $a(z, s)$ is the appropriate functions to be determined next. The ionic flux in the x direction can be expressed as[48]

$$f(x,z,s) = -D\left(\frac{1}{F}\frac{\partial \rho(x,z,s)}{\partial x} - \frac{FC_0}{RT}E(x,z,s)\right), \quad (43)$$

where R is the gas constant, and T is the absolute temperature. Considering the boundary condition as

$$f(h,z,s) = f(-h,z,s) = 0. \quad (44)$$

Since $E(\pm h, z, s) \neq 0$, by solving Eq. (43), one can obtain

$$\begin{aligned} E(x,z,s) =& 2\hat{C}(s)\frac{(L-z)\cosh(A(s)x)}{\hat{\varepsilon}A(s)} \\ &+ 2\hat{C}(s)(L-z)\cosh(A(s)h)\left(\frac{RTA(s)}{F^2C_0} - \frac{1}{\hat{\varepsilon}A(s)}\right). \end{aligned} \quad (45)$$

Then the ionic flux is

$$\begin{aligned} f(x,z,s) = &-2D\hat{C}(s)(L-z)(\cosh(A(s)x) \\ &+ \cosh(A(s)h))\left(\frac{A(s)}{F} - \frac{FC_0}{RT\hat{\varepsilon}A(s)}\right). \end{aligned} \quad (46)$$

By using Ramo-Shockley theorem, the local current density at an electrode boundary can be expressed as

$$\begin{aligned} j(z,s) &= \frac{1}{h}\int_{-h/2}^{h/2} f(x,z,s)dx \\ &= -\frac{2D\hat{C}(s)(L-z)}{h}\left(\frac{\sinh(A(s)h)}{A(s)} + h\cosh(A(s)h)\right) \\ &\quad \times \left(\frac{A(s)}{F} - \frac{FC_0}{RT\hat{\varepsilon}A(s)}\right). \end{aligned} \quad (47)$$

C. Electric potential on the electrodes

To study the electric potential in the electrode, Ohm's law for the current density of the electrodes is utilized and is denoted as[27]

$$\varphi\nabla V = -\vec{j}, \quad (48)$$

where φ is the electric conductivity and the following equation is true:

$$\varphi(t) = \frac{L}{2R_e(t)Wh_e}. \quad (49)$$

By converting the integration of current density into time domain by inversing the Laplace transformation, the electrode potential of the compressed electrode can be donated as

$$V(t) = -\frac{1}{\varphi(t)} F^{-1}\left\{ \int_0^L j(z,s)dz \right\}. \tag{50}$$

III. EXPERIMENTAL VALIDATION

We studied the electrical properties of the IPMC sensor electrode. Based on the SEM images, the microstructure of the IPMC electrode was shown. An experimental apparatus was developed to test the impedance of the electrodes. The resistance, capacitance, and surface electric potential of the IPMC sensor electrode were measured in the system. Finally, the experimental results were compared with the simulation results to validate the model.

A. Experimental set up

Six IPMC strips with different electrode thicknesses, manufactured by Environmental Robots, Inc., were utilized in the experiments. The SEM was used to study the structure of the IPMC. Figure 4 shows the cross-sectional images of the IPMC indicating the platinum content distribution in the electrode and vicinity. It can be seen that the IPMC was composed of the upper electrode, the polymer membrane, and the inner electrode between them. The upper electrode, where the metal particles are electrically connected, mainly results in the resistance and cannot form a capacitor. The inner electrode, where the metal particles are insulated by Nafion, can build capacitors. In the model, the electrodes are considered a bulk metal. However, in reality from the SEM images, it can be seen that the structure is more complicated. The thickness of the electrode could vary significantly. The thin electrolessly plated electrodes on a polymer do not result in a uniform conductivity in each direction at each location, so the defective cube factor helps to take those effects into account. With the SEM images, the parameters of the electrode can be measured, which were shown in Table I. To validate the model, IPMC strips with different electrode thickness were chosen in the current study.

An illustration of the experimental apparatus is shown in Fig. 5(a), while Fig. 5(b) shows the actual picture during the experiment. A crank-slider mechanism was used to convert the rotational motion generated by a DC motor (36SYK71, Saegmotor Co., China) into the linear, oscillatory motion of the slider while sliding on a fixed rail. The slider was fixed to another slider containing a rail inside vertically at one end. A nail fixed at the rotating disk slides on the rail of the slider. The amplitude of the translational motion can be adjusted by changing the distance from the nail to the disk center. A motor controller (BDMC4810, Beijing UPTECH Robotics Co. Ltd, China) was used to monitor the motor based on the voltage input and the encoder feedback. By utilizing the Personal Computer (PC) to send the orders to the motor controller, the oscillation frequency is controlled. The apparatus can provide the periodic excitation which varies from 0.01 Hz to 2 Hz and 2.5 mm to 15 mm. A laser sensor (OADM 20U2441/S14C, Baumer, Inc., Switzerland) was used to calibrate the apparatus.

The clamp at the end of the slider constrained the free end of a cantilevered IPMC beam. The tip-bending deformation of the IPMC beam was correlated with the slider motion. During the experiments, the contact point between the IPMC beam and the slider changed slightly. For relatively small oscillation amplitude, the contact point was treated as fixed and near the beam tip. In the experiments, the oscillation amplitude, D_a, was chosen between 5 mm and 15 mm.

A circuit, which connected the two ends at the one side of the IPMC, was used to test the properties of the IPMC electrode under the mechanical stimulus. Different circuits were chosen for the separate measurement of the resistance, capacitance, and electric potential of the IPMC electrode. A data recorder (Nicolet Vision XP, LDS Inc., Germany) was used to record the experimental results, which has 16 sampling channels and a maximum sampling rate of 100 kHz.

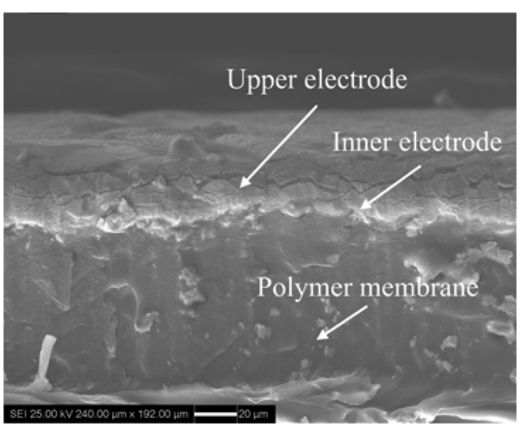

FIG. 4. Cross-sectional SEM images of the IPMC 1.

B. Resistance

The circuit for measuring the resistance of the IPMC electrode consisted of a stabilized voltage supply of 2 V and a 10 Ω resistor in the series (see Fig. (5)). In our study, the IPMC oscillated at the frequency of 0.4 Hz, 1 Hz, and 1.6 Hz, and at the amplitudes of 5 mm, 7.5 mm, and 10 mm, respectively. The data recorder was used to record the voltage of the electrode, V_{er}, and the voltage of the resistor, V_{rr}. The current in the electrode is the same as the current in the resistor in the series circuit and can be obtained as

$$I_{er} = \frac{V_{rr}}{10}. \tag{51}$$

Then the resistance of the electrode is presented as

$$R_e = \frac{V_{er}}{I_{er}} = \frac{10V_{er}}{V_{rr}}. \tag{52}$$

The recorded experimental data was analyzed in a computer using MATLAB. To validate the model, the parameters need to be identified. Some are physical constants, such as R and F. The values can be found in Ref. 27. Some can be measured directly, such as temperature, dimensions of IPMC. The others need to be identified through curve-fitting using the least-square method. In the current study, the microstructure of the IPMCs' platinum electrode is face-centered. Based on

TABLE I. Dimensions of IPMC samples.

Item	IPMC 1	IPMC 2	IPMC 3	IPMC 4	IPMC 5	IPMC 6
Length (mm)	51.89	50.58	34.46	38.54	28.46	42.20
Width (mm)	7.40	8.24	9.62	9.44	9.30	10.84
Thickness (mm)	0.30	0.26	0.27	0.29	0.28	0.30
Upper electrode thickness (μm)	10.67	16.85	8.81	11.86	7.53	9.94
Inner electrode thickness (μm)	1.28	1.50	1.15	1.33	0.89	1.15

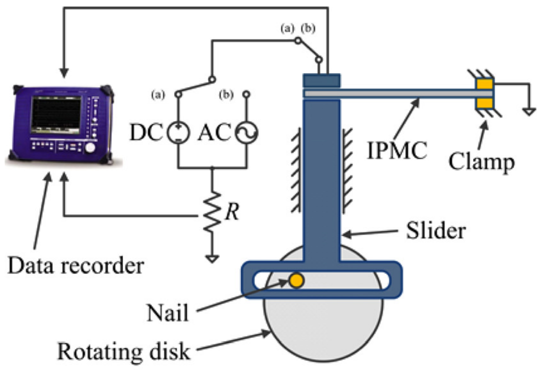

(a)

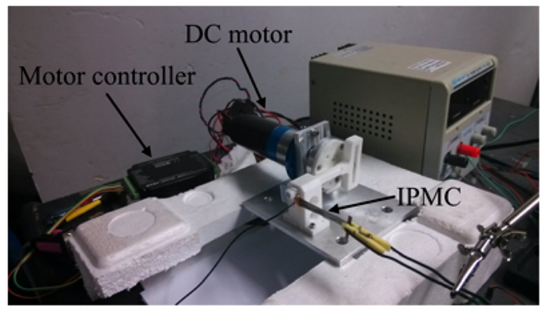

(b)

FIG. 5. (a) Schematic illustration of the experimental set up; (b) snapshot of the experimental apparatus.

the least-square error analysis of the experimental results, the parameters of the model were identified. Figure 6 shows the comparison between simulation results and experimental results of the electrode resistance. It can be seen that under the sinusoidal tip displacement of the IPMC beam, the resistance of the electrode shows a sinusoidal variation. It can be found that the simulation results of the electrode model match well with the electrode resistance. Figure 7 shows the resistance and the resistance change of the IPMC electrodes. The simulation results and experimental results were compared. It is shown that the model can well describe the resistance of the electrode. It is also noticed that with the amplitude of the tip displacement increasing, the resistance change of the electrode increased. Shahinpoor and Kim reported a novel fabrication process of manufacturing IPMCs equipped with physically loaded electrodes. Similar surface resistance results were measured on the IPMCs.[49]

C. Capacitance

To measure the capacitance of the IPMC electrode, an alternating circuit was proposed. An alternating current (AC) power supply which has a square signal with a peak voltage of 2 V and frequency of 1000 Hz was utilized. A resistor of 10 Ω was in series with the electrode for the measurement of the current, as shown in Fig. 5. The oscillation frequency and the amplitude of the IPMC were the same as that of the resistance measurement. The voltage of the electrode, V_{ec}, and the voltage of the resistor, V_{rc}, in the experiments were measured. The current in the electrode is presented as

$$I_{ec} = \frac{V_{rc}}{10}. \tag{53}$$

Based on the definition of the capacitance, the capacitance of the electrode can be expressed as

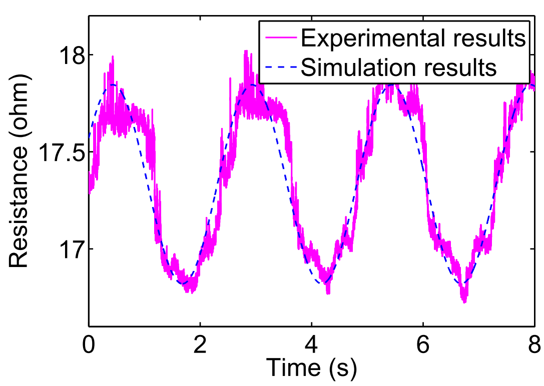

(a)

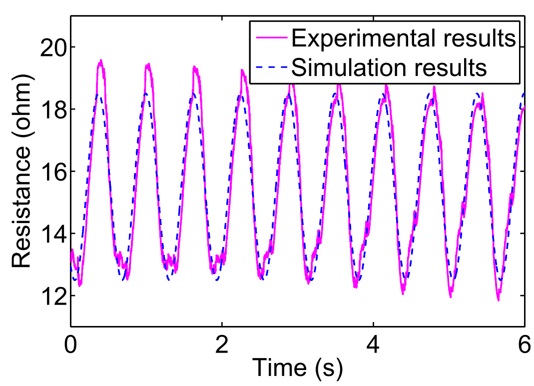

(b)

FIG. 6. Comparison between the simulation results and experimental results of the electrode resistance: (a) IPMC 2 at an oscillation amplitude of 5 mm and a frequency of 0.4 Hz. (b) IPMC 4 at an oscillation amplitude of 7.5 mm and a frequency of 1.6 Hz.

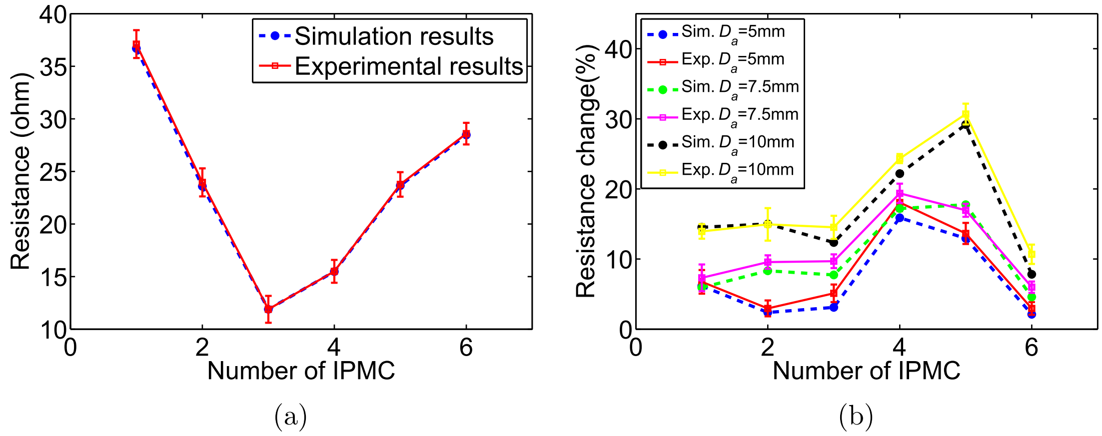

FIG. 7. Comparison between the simulation results and experimental results of the electrode: (a) Resistance of IPMCs' electrode. (b) Resistance change of the IPMCs' electrode at different oscillation amplitudes.

$$C_{ec} = \frac{Q_e}{V_e} = \frac{\frac{1}{2}\int_{t_s}^{1/\hat{f}+t_s}(I_{ec} - I_r)dt}{V_e}, \tag{54}$$

where t_s is a time point when the output voltage of the AC power supply alternated, $\hat{f}$ is the frequency of the alternating circuit, V_e is the peak voltage of the electrode in the steady state, and I_r is the current caused by the resistance of the electrode and is presented as

$$I_r = \frac{V_{ec}}{R_e}. \tag{55}$$

Apart from the parameters that are physical constants and can be measured directly, the other parameters need to be identified based on the experimental results. The least-square error analysis was performed in the MATLAB, and the parameters of the model were identified. Figure 8 shows the comparison between the simulation results and experimental results of the electrode capacitance. Like the results of the resistance, it is shown that the capacitance of the electrode shows a sinusoidal change under the sinusoidal oscillation. A plausible agreement was achieved between the simulation results of the electrode model and the electrode resistance, and Fig. 9 shows the validation of the model in describing the capacitance of the IPMC electrode. The simulation results match well with the experimental results. It is also found that the capacitance change of the electrode increases as the tip displacement increases.

D. Surface electrical potential

We measured the surface potential of the IPMC as the last test. The IPMC beams were under the same mechanical stimulation as before. Some parameters of the model were based on previous results such as the resistance parameters. Some need to be identified such as the polymer membrane parameters. The surface voltages of the IPMC beams were measured, and the parameters of the model were identified. Figure 10 gives the comparison between the simulation results and experimental results of the electrode at different conditions. The simulation results and the experimental results of the surface potential match well. A sinusoidal change was also tested due to the sinusoidal oscillation of the IPMC. Figure 11 shows the simulation results and experimental results of the surface electrical potential. It can be found that the model can well describe the surface electrical potential of the IPMC beams. The surface electrical potential also increases with the amplitude of the IPMC increases.

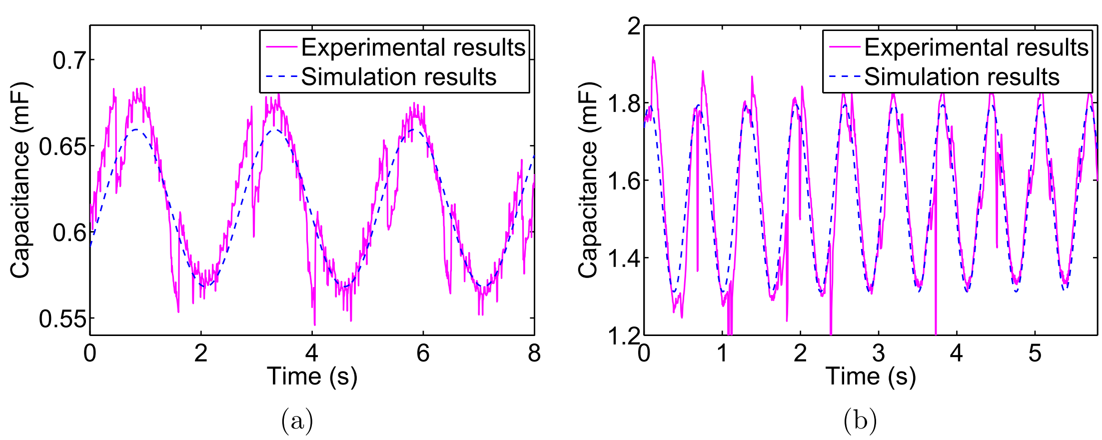

FIG. 8. Comparison between the simulation results and experimental results of the electrode capacitance: (a) IPMC 2 at the oscillation amplitude of 5 mm and frequency of 0.4 Hz. (b) IPMC 3 at the oscillation amplitude of 7.5 mm and frequency of 1.6 Hz.

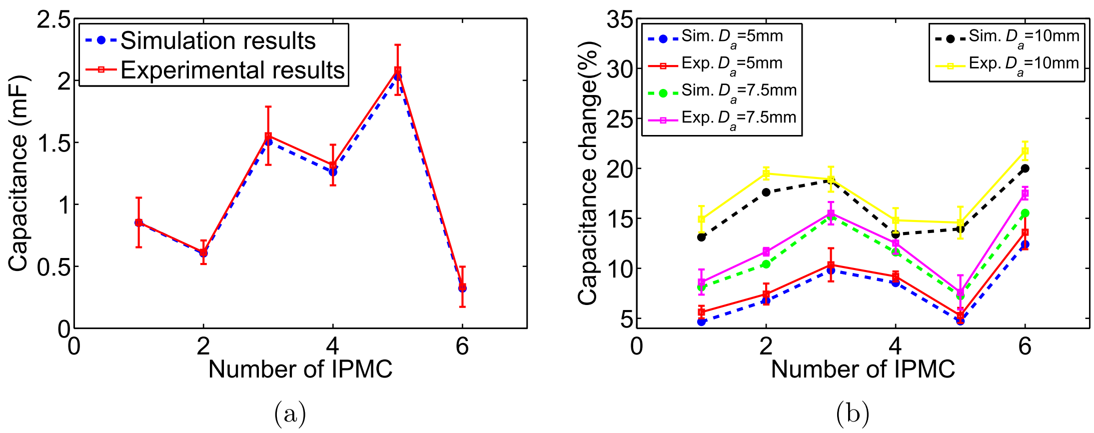

FIG. 9. Comparison between the simulation results and experimental results of the electrode: (a) Capacitance of IPMCs' electrode. (b) Capacitance change of the IPMCs' electrode at different oscillation amplitude.

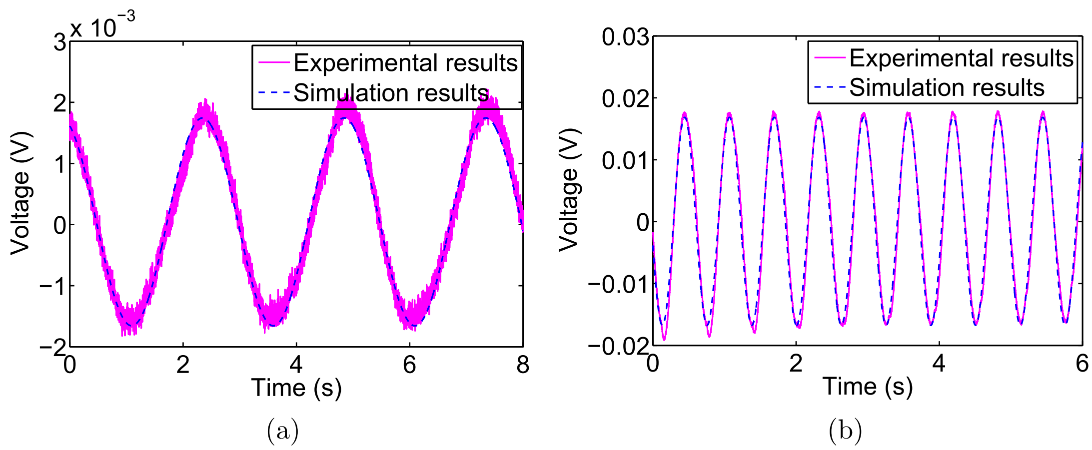

FIG. 10. Comparison between the simulation results and experimental results of the electrode: (a) IPMC 5 at the oscillation amplitude of 5 mm and frequency of 0.4 Hz; (b) IPMC 3 at the oscillation amplitude of 10 mm and frequency of 1.6 Hz.

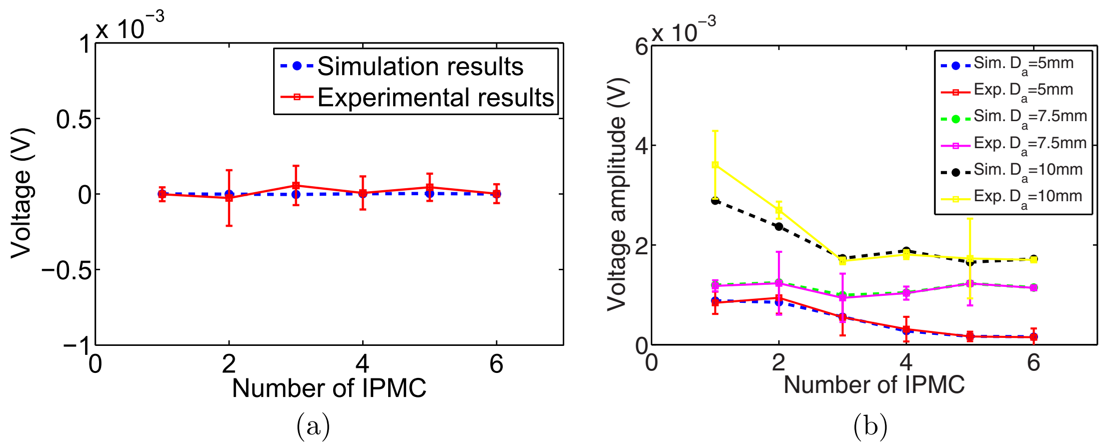

FIG. 11. Comparison between the simulation results and experimental results of the electrode: (a) surface potential of IPMCs' electrode; (b) surface potential amplitude of the IPMCs' electrode at different oscillation amplitude.

IV. DISCUSSION

A. Resistance

Since the dimensions and electrode parameters of the IPMC samples above were different from each other, the comparison of their experimental results is unsuitable for understanding the electrical properties of the IPMC electrode. In this paper, simulations were performed based on the validated model for the investigation of the electrode. The dimensions of the model are: length $L = 22$ mm, width $W = 7$ mm, thickness $2h = 0.3$ mm. The thickness of the upper electrode is 20 μm. The others are based on the previous experimental results. The simulation results of the resistance are shown as follows. Based on Fig. 12, the electrode thickness, percent of missing particles, and resistivity of plated metal have a major effect on the resistance of the electrode. With Fig. 12(a), we found that as the particle diameter increases, the resistance of the electrode has a relatively low decrease. The electrode resistance decreases as the electrode thickness increases based on Fig. 12(b). It can be seen from Fig. 12(c) that the resistance has a rise as the contact area ratio of the particle increases. The electrode resistance increases rapidly as the percent of the missing particles increases with Fig. 12(d). It is also noticed that the electrode resistance shows a linear rise as the resistivity of the metal increases from Fig. 12(e). Similar results were found in Ref. 40.

B. Capacitance

Based on the model developed above, a simulation was performed to study the capacitance of the electrode. The thickness of the inner electrode is 1 m. The other parameters of the model were the same as above. The simulation results of the capacitance are shown as follows. Based on Fig. 13, it can be indicated that the electrode thickness, percent of missing particles, and the gap between particles have major effect on the capacitance of the inner electrode. From Fig. 13(a), it

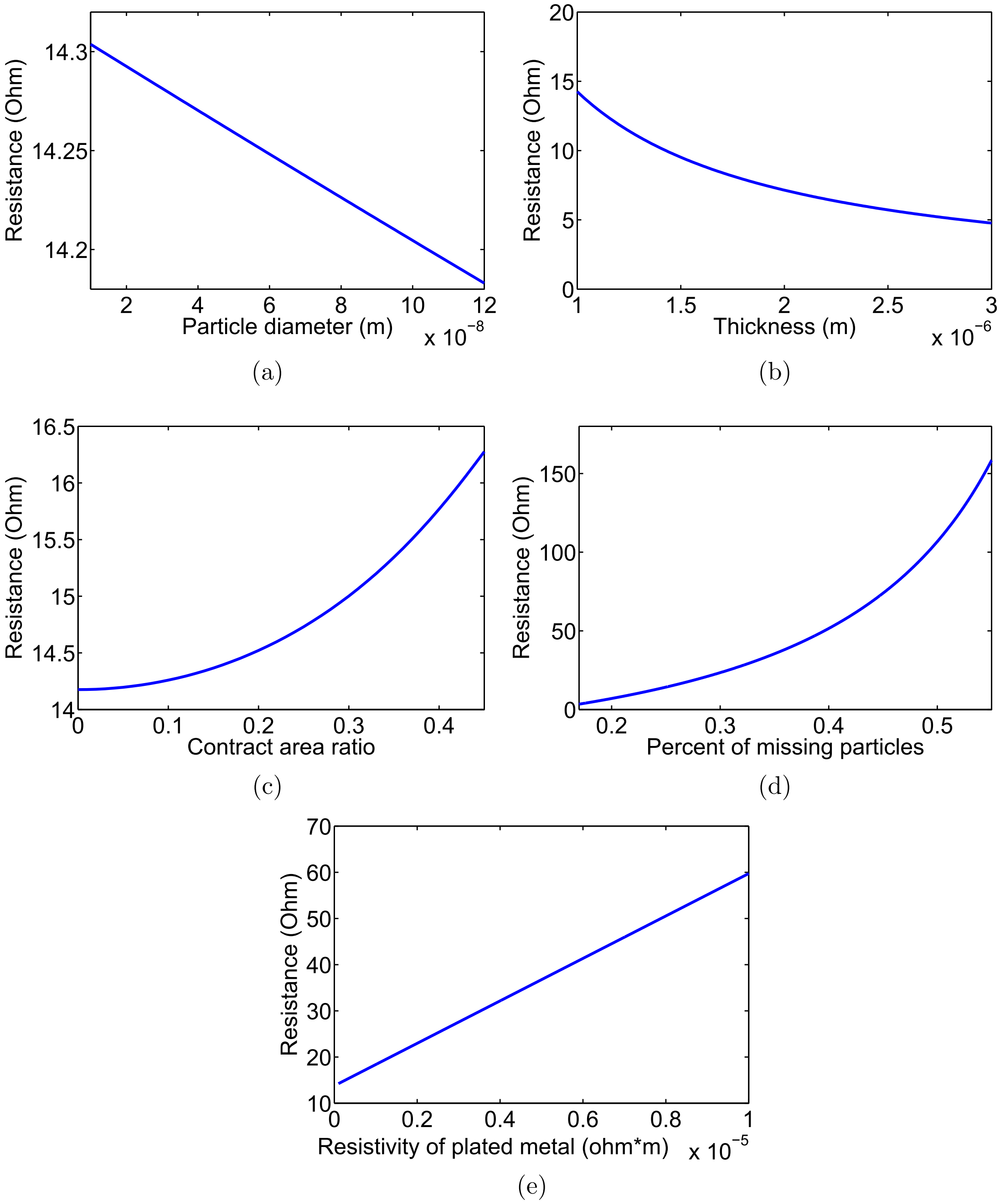

FIG. 12. Modeling of electrode resistance versus (a) particle diameter, (b) electrode thickness, (c) particle contract area, (d) percent of missing particles, (e) resistivity of plated metal.

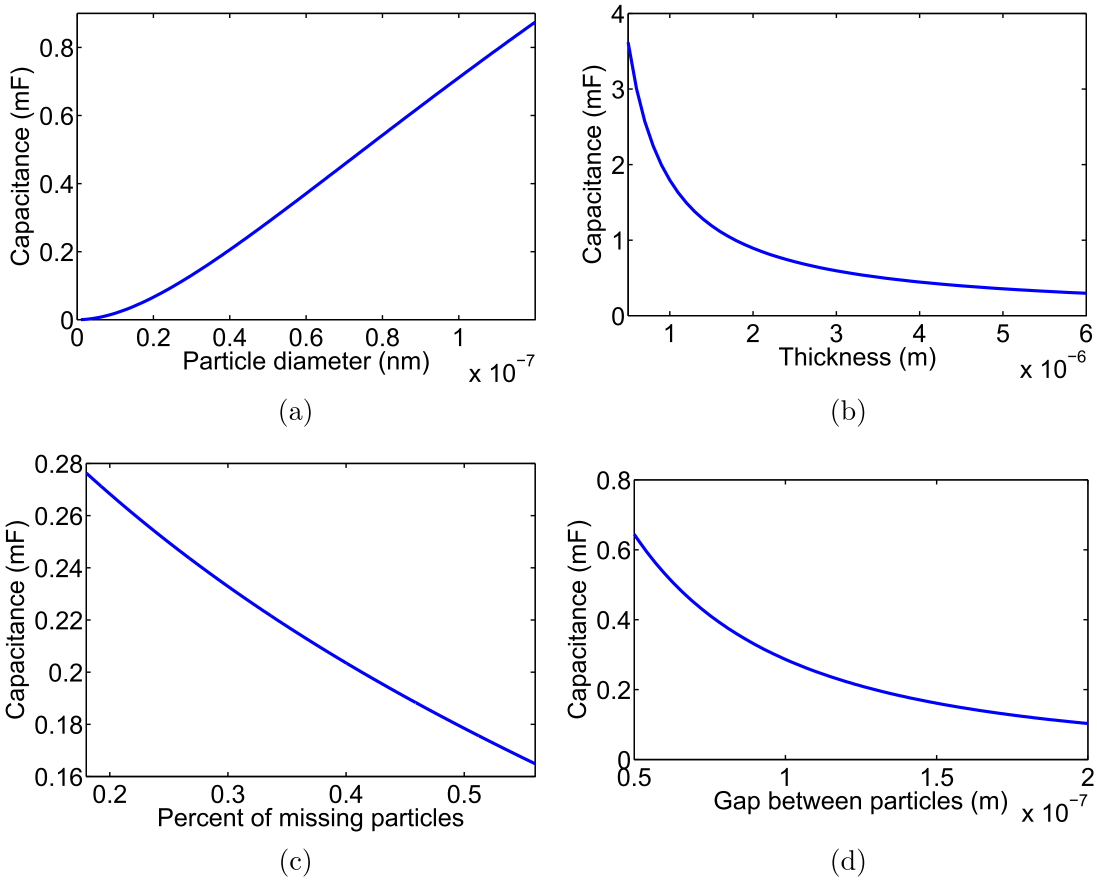

FIG. 13. Modeling of electrode capacitance versus (a) particle diameter; (b) electrode thickness; (c) percent of missing particles; (d) gap between particles.

is found that the capacitance of the electrode increases as the particle diameter increases. The electrode capacitance decreases as the inner electrode thickness increases in Fig. 13(b). Figure 13(c) shows that with the percent of the missing particles increasing, the electrode capacitance decreases slowly. It is noticed in Fig. 13(d) that the electrode capacitance decreases as the gap between particles increases. Similar results were also shown in Ref. 40.

C. Surface voltage

We performed the simulation of the surface potential based on the above model. The voltage on the surface of the electrode of the IPMC sensor is shown in Fig. 14. It can be found that the electrode thickness, percent of missing particles, and the resistivity of the plated metal have a major effect on the surface potential of the electrode. The surface voltage amplitude has a linear decrease as the particle diameter increases based on Fig. 14(a). In Fig. 14(b), the surface voltage amplitude rises gently as the thickness of the electrode increases. It is also found that the surface voltage amplitude increases rapidly as the contact area ratio and the percent of missing particles increases based on Figs. 14(c) and 14(d). Figure 14(e) shows that the surface voltage amplitude rises linearly as the resistivity of the plated metal increases.

D. Microstructure of the electrode

Finally, we study the influence of the microstructure on the electrode properties. The parameters for the models are based on previous work and are the same. Table II shows the simulation results of the three microstructures. It is shown that the FCC and HCP structures result in a high electrode resistance and are close to each other. The BCC shows a low electrode resistance. When it comes to the capacitance, it is the reverse situation. The electrode has the highest capacitance at the BCC. It is lower with the FCC and HCP structures. The results of the surface potential show a similar situation with the resistance. The surface potential of the FCC and HCP structures is relatively high and are close to each other. While the BCC produces a lower surface potential. By current study, one can change the parameters of the IPMC electrode during the fabrication process to achieve the necessary electrode properties.

V. CONCLUSIONS

In this study, we focus on the modeling of IPMC sensor. A microstructure model of the electrode and a model of the IPMC surface potential were developed. Experiments were then performed to validate the model. The theoretical results and the experimental results show a good agreement. A parametric study was done to observe the electrode properties of the IPMC sensors. The resistance, capacitance, and the surface potential of the IPMC electrode were presented. The results show that parameters such as the particle diameter, the electrode thickness, and the percent of missing particles have a major influence on the electrical properties of the IPMC electrode. By changing the parameters, its electrical

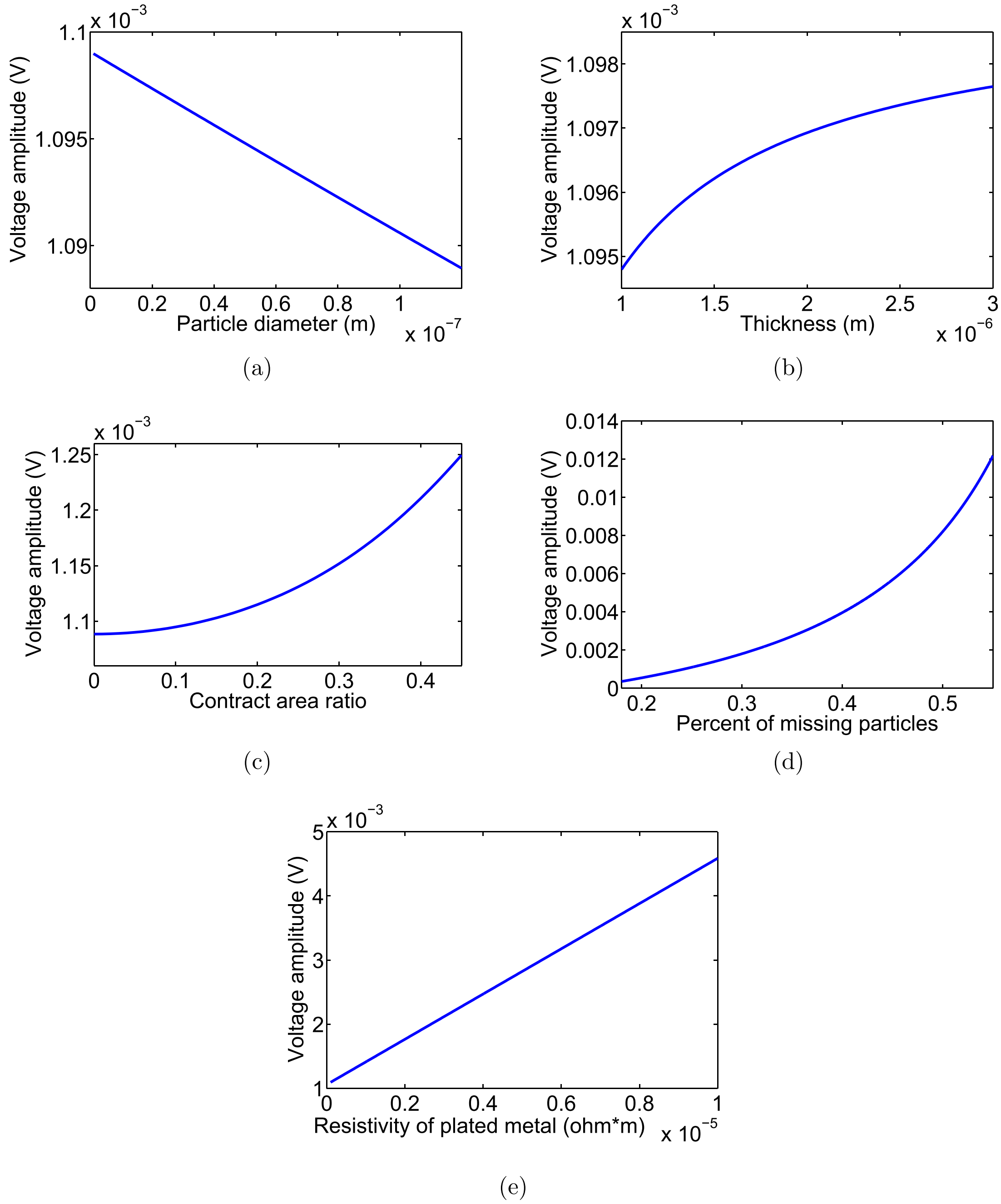

FIG. 14. Modeling of surface potential amplitude versus (a) particle diameter; (b) electrode thickness; (c) particle contract area; (d) percent of missing particles; (e) resistivity of plated metal.

characteristics can be changed. We also compared the electrode properties for three microstructures. It is found that the FCC and HCP structures show relatively high resistance and surface potential. The BCC shows relatively high capacitance. The current study is beneficial for better understanding the electrical characteristics of the IPMC electrode. This method of modeling and the experimental apparatus may also be useful in studying the electrode of other smart materials.

TABLE II. Simulation results of the three microstructures.

Item	FCC	BCC	HCP
Resistance (Ω)	14.26	3.14	13.24
Capacitance (mF)	0.29	0.69	0.22
Surface potential (mV)	1.10	0.24	0.99

This paper focuses on the electrical properties of the IPMC electrode. However, its influence on the sensing and actuating performance has not been completely learned. In the future, we will study the non-linear properties of the IPMC sensor/actuator with the effect of the electrode.

ACKNOWLEDGMENTS

Many thanks to Lei Bao and Zhongyu Wang for their help during the experimental investigation. This work was in part supported by National Natural Science Foundation of

China (No. 61075100) (Q.S. and T.W.). Also, this material is based in part upon work supported by the U.S. National Science Foundation under Grant No. 1265123 (K.J.K.).

[1]K. A. Morgansen, B. I. Triplett, and D. J. Klein, IEEE Trans. Rob. **23**, 1184 (2007).
[2]J. Yu, Y. Fang, W. Zhao, and L. Wang, in *IEEE International Conference on Robotics and Biomimetics (ROBIO)* (2005), pp. 472–477.
[3]M. G. Borgen, G. N. Washington, and G. L. Kinzel, IEEE/ASME Trans. Mechatron. **8**, 66 (2003).
[4]C. Rossi, W. Coral, J. Colorado, and A. Barrientos, in *IEEE International Conference on Robotics and Automation (ICRA)* (2011), pp. 3646–3651.
[5]J. Tangorra, P. Anquetil, T. Fofonoff, A. Chen, M. Del Zio, and I. Hunter, Bioinspiration Biomimetics **2**, S6 (2007).
[6]X. Tan, Mar. Technol. Soc. J. **45**, 31 (2011).
[7]V. I. Fernandez, S. M. Hou, F. S. Hover, J. H. Lang, and M. S. Triantafyllou, Development and application of distributed MEMS pressure sensor array for AUV object avoidance (Massachusetts Institute of Technology, Sea Grant College Program, 2009).
[8]Y. Yang, N. Nguyen, N. Chen, M. Lockwood, C. Tucker, H. Hu, H. Bleckmann, C. Liu, and D. L. Jones, Bioinspiration Biomimetics **5**, 016001 (2010).
[9]A. Giacomello and M. Porfiri, J. Appl. Phys. **109**, 084903 (2011).
[10]Q. Shen, T. Wang, L. Wen, and J. Liang, Int. J. Adv. Robot. Syst. **10**, 350 (2013).
[11]T. Wang, Q. Shen, L. Wen, and J. Liang, Sci. China Technol. Sci. **55**, 3359–3369 (2012).
[12]Q. Shen, T. Wang, J. Liang, and L. Wen, Smart Mater. Struct. **22**, 075035 (2013).
[13]B. Bhandari, G.-Y. Lee, and S.-H. Ahn, Int. J. Precis. Eng. Manuf. **13**, 141 (2012).
[14]D. Pugal, K. J. Kim, A. Punning, H. Kasemägi, M. Kruusmaa, and A. Aabloo, J. Appl. Phys. **103**, 084908 (2008).
[15]S. Nemat-Nasser, S. Zamani, and Y. Tor, J. Appl. Phys. **99**, 104902 (2006).
[16]S. Nemat-Nasser and S. Zamani, J. Appl. Phys. **100**, 064310 (2006).
[17]S. Nemat-Nasser and Y. Wu, J. Appl. Phys. **93**, 5255–5267 (2003).
[18]S. Nemat-Nasser, J. Appl. Phys. **92**, 2899–2915 (2002).
[19]M. Aureli, W. Lin, and M. Porfiri, J. Appl. Phys. **105**, 104911 (2009).
[20]M. Shahinpoor and K. J. Kim, Smart Mater. Struct. **10**, 819 (2001).
[21]M. Shahinpoor and K. J. Kim, Smart Mater. Struct. **14**, 197 (2005).
[22]P. De Gennes, K. Okumura, M. Shahinpoor, and K. Kim, Europhys. Lett. **50**, 513 (2000).
[23]M. Shahinpoor and K. J. Kim, Smart Mater. Struct. **9**, 543 (2000).
[24]S. Nemat-Nasser and J. Y. Li, J. Appl. Phys. **87**, 3321 (2000).
[25]Z. Chen and X. Tan, IEEE/ASME Trans. Mechatron. **13**, 519 (2008).
[26]M. Porfiri, Phys. Rev. E **79**, 041503 (2009).
[27]D. Pugal, K. J. Kim, and A. Aabloo, J. Appl. Phys. **110**, 084904 (2011).
[28]M. Shahinpoor, in *Smart Structures & Materials' 95* (1995), pp. 42–53.
[29]M. Shahinpoor, Y. Bar-Cohen, J. Simpson, and J. Smith, Smart Mater. Struct. **7**, R15 (1998).
[30]M. Shahinpoor, *Polymer Sensors and Actuators* (Springer, 2000), pp. 325–359.
[31]M. Shahinpoor and M. Mojarrad, U.S. patent 6,475,639 (5 November 2002).
[32]M. Shahinpoor, K. J. Kim, B. K. Henderson, and D. J. Leo, in *SPIE's 8th Annual International Symposium on Smart Structures and Materials* (2001), pp. 267–274.
[33]A. Keshavarzi, M. Shahinpoor, K. J. Kim, and J. W. Lantz, in *Symposium on Smart Structures and Materials* (1999), pp. 369–376.
[34]K. J. Kim, M. Shahinpoor, and A. Razani, in *SPIE's 7th Annual International Symposium on Smart Structures and Materials* (2000), pp. 311–320.
[35]K. Farinholt and D. J. Leo, Mech. Mater. **36**, 421 (2004).
[36]C. Bonomo, L. Fortuna, P. Giannone, S. Graziani, and S. Strazzeri, Smart Mater. Struct. **15**, 749 (2006).
[37]Z. Chen, X. Tan, A. Will, and C. Ziel, Smart Mater. Struct. **16**, 1477 (2007).
[38]M. Aureli and M. Porfiri, Continuum Mech. Thermodyn. **25**, 273 (2013).
[39]R. Tiwari and K. Kim, Smart Mater. Struct. **22**, 015017 (2013).
[40]S. J. Kim, S.-M. Kim, K. J. Kim, and Y. H. Kim, Smart Mater. Struct. **16**, 2286 (2007).
[41]S. Dannefaer, P. Mascher, and D. Kerr, Phys. Rev. Lett. **56**, 2195 (1986).
[42]E. Martínez and C.-C. Fu, Phys. Rev. B **84**, 014203 (2011).
[43]D. Backlund and S. Estreicher, Phys. Rev. B **81**, 235213 (2010).
[44]L. Ismer, M. S. Park, A. Janotti, and C. G. Van de Walle, Phys. Rev. B **80**, 184110 (2009).
[45]S. Ramo, Proc. IRE **27**, 584 (1939).
[46]H. Barrett, J. Eskin, and H. Barber, Phys. Rev. Lett. **75**, 156 (1995).
[47]R. Tiwari and K. J. Kim, Appl. Phys. Lett. **97**, 244104 (2010).
[48]M. Porfiri, J. Appl. Phys. **104**, 104915 (2008).
[49]M. Shahinpoor and K. J. Kim, Sens. Actuators, A **96**, 125–132 (2002).